Enhanced Photogenerated Charge Carriers and Photocatalytic Activity of Biotemplated Mesoporous TiO 2 Films with a Chiral Nematic Structure

Getaneh Diress Gesesse, Chunyu Li, Erwan Paineau, Youssef Habibi, Hynd Remita, Christophe Colbeau-Justin, Mohamed Nawfal Ghazzal

Enhanced photogenerated charge carriers and photocatalytic activity of biotemplated mesoporous TiO_2 films with a chiral nematic structure

*Getaneh Diress Gesesse[†], Chunyu Li[†], Erwan Paineau[‡], Youssef Habibi[∓], Hynd Remita[†], Christophe Colbeau-Justin[†], Mohamed Nawfal Ghazzal *[†]*

[†] Laboratoire de Chimie Physique, UMR 8000 CNRS, Université Paris-Sud, Université Paris-Saclay 91405 Orsay, France
[‡] Laboratoire de Physique du Solide, UMR 8502 CNRS, Université Paris-Sud, Université Paris-Saclay 91405 Orsay, France
[∓] Department of Materials Research and Technology (MRT), Luxembourg Institute of Science and Technology (LIST), 5 avenue des Hauts-Fourneaux, L-4362 Esch-sur-Alzette, Luxembourg

ABSTRACT: Photogeneration and lifetime of charge carriers associated to light harvesting are among the main challenges facing materials for photocatalysis. We report here the synthesis of mesoporous TiO_2 containing a replica of a chiral nematic structure (CNs) as a photocatalyst with improved light harvesting and photogenerated charge carriers under UV illumination. The CNs of cellulose nanocrystals photonic films, obtained by evaporation induced self-assembly method, were successfully transferred into an inorganic TiO_2 film by sol-gel mineralization of the biotemplate. The stop-band of the photonic films was adjusted by controlling the amount of added D-glucose. The improvement of the kinetics of phenol photocatalytic degradation, H_2 production and the enhancement of the TiO_2 photoconductivity as measured by Time Resolved Microwave Conductivity, compared to mesoporous TiO_2, strongly suggest an increase in light harvesting. The CNs microdomains in TiO_2 increase the light scattering within the nanostructure, and thus the absorption factor of TiO_2 resulting in higher photoefficiency. This peculiar structure is used for the deposition of gold nanoparticles (AuNPs) inside the mesopores that are left by the mineralization of the biotemplate. AuNPs act as co-catalysts by leveraging highly photogenerated charge carriers for the production of H_2. This straightforward method opens up new opportunities, especially for a wide range of materials, where converting photons into energy remains a major challenge.

Titanium dioxide is a semiconductor that is commonly used in a wide range of applications such as photocatalysis,[1–3] dye sensitized solar cells,[4–6] hygrochromic coatings,[7,8] sensor materials [9,10] and mesoporous optical Bragg stacks [11,12]. In its anatase form, TiO_2 is by far the most popular photocatalyst used in environmental applications. However, its large band gap (3.2 eV for anatase), which can only be excited with UV light, combined with a high recombination rate of the photogenerated electron/hole pairs (e^-/h^+), reduces both the light harvesting ability and the photon-to-charge carriers conversion efficiency. Different strategies have been therefore explored to overcome these limitations with more or less success. One consists in doping TiO_2 with non-metallic elements,[13–15] while others focus on coupling TiO_2 with metallic nanoparticles,[16–18] noble metals[3,19–22] or narrow band-gap semiconductors.[23] Although these strategies extend the absorbance of TiO_2 in the visible range while improving the lifetime of the charge carriers, they fail to induce an effect on the photogenerated (e^-/h^+) density under UV illumination. In the meantime, the use of plasmonic nanoparticles (NPs) has emerged over the past decade as an effective and innovative method to improve the light harvesting of TiO_2 photocatalyst. In particular, NPs act as electron collectors, reducing the recombination efficiency of charge carriers or improving the light harvesting of the TiO_2 photocatalyst by injecting hot electrons coming from localized surface plasmon resonance (LSPR) into the TiO_2 conduction band (making the visible light useable).[20,22,24] However, the LSPR intensity remains insufficient to effectively collect the light received by the photocatalyst.

Improving light harvesting (i.e. increasing the absorbance factor) of TiO_2 photocatalyst becomes therefore a challenge, especially with regard to the management of light propagation. Indeed, photons pass through nanosized photocatalyst particles with a light velocity around $1-3 \times 10^8$ $m.s^{-1}$, leaving less than a hundred femtoseconds to TiO_2 for its activation. The confinement of light in a hierarchical structure should reduce the time of light propagation by multiple light scattering

phenomena leading, in principle, to a better light harvesting. Hierarchical structures with a periodic arrangement (photonic crystals)[6] or a less regular arrangement (spongy mesophyll cells)[25] present a very efficient light harvesting for photon-to-energy conversion. In this context, hierarchical structures inspired by Nature (biomimetics) show a growing interest in this kind of applications. It is well recognized that the hierarchical structures of living species exibit an amazing ability to handle light for vital or energy needs. For instance, the hierarchical structures of green leaves are designed for light harvesting towards an efficient conversion of photons into chemical energy.[26] By mimicking natural hierarchical structures, porous bioinspired TiO_2 materials containing a well-defined hierarchical structure (including small replicas of chloroplast structures) were obtained using the plant leaves as biotemplates. The bioinspired TiO_2 material is of interest for photocatalytic reaction, in particular dye degradation and H_2 production.[27,28] Natural photonic crystals (PCs) found in Nature, e.g. butterfly wings,[29,30] Pollia,[31] opals or beetle cuticles,[32,33] represent unique but complex arrangements that manage the propagation of light in such a perfect way that they produce iridescent colours. Upon irradiation, the group velocity of photons near the photonic band-gap edges is significantly reduced (slow photon effect), which could improve the absorbance factor of the photocatalyst. The beneficial effect of slowing down photons was first revealed in dye-sensitized solar cells. Opal TiO_2 layers periodically structured in 3D photonic lattice have improved the photogenerated current.[6] The photoefficiency has been shown to be wavelength-dependent, since the irradiation wavelength should correspond to the absorbance range of the photocatalyst.[2,4,34-36] PCs are now accepted as an effective strategy to increase the photon-to-electron conversion for next-generation dye-sensitized solar cells.[4,36] But so far, most of these studies have been carried out only using synthetic photonic TiO_2 from opal and inverse opal templates.

Since the pioneering work of Dujardin,[37] cellulose nanocrystals (CNCs) have emerged as straightforward biotemplates to produce mesosoporous metal-oxides assemblies with chiral nematic structures.[38–41] TiO_2 nanocrystalline films with a chiral nematic structure organization were first elaborated from mesoporous silica with chiral nematic ordering by hard templating.[40] However, to be effective, this approach requires repeating the impregnation/calcination steps at high temperature. Between each step, etching to remove the CNC-silica template is mandatory. This method is efficient, but time-consuming and can leave sodium ions in the TiO_2 nanostructure during the etching of the silica template, which may have a detrimental effect on the resulting photocatalytic activity.[42–44]

In this work, we report synthesis of mesoporous biotemplated TiO_2 containing a replica of a chiral nematic structure using an impregnation method. The chiral nematic structure of cellulose nanocrystals photonic films was successfully transferred to inorganic TiO_2 films by an approach combining soft chemistry and evaporation induced self-assembly (EISA) method. The photonic stop-band of the resulting biotemplated TiO_2 films was adjusted by controlling the amount of added D-glucose. This straightforward method facilitates the transfer of the replica of the chiral nematic structure to TiO_2. The resulting chiral nematic mesoporous ($CNTiO_2$) films enhanced light harvesting with higher photoefficiency than pristine mesoporous TiO_2. In addition, we have shown that the mesopores left by the mineralization of CNCs also allow the deposition of gold nanoparticles offering the possibility of using these materials for an efficient H_2 production.

EXPERIMENTAL

Materials

Titanium isopropoxide (TTiP, 97 %), Acetylacetone (acac, 97%), D-glucose, methanol (Reagentplus, ≥99%) and phenol (C_6H_5OH) obtained from Aldrich, Acetic acid (CH_3COOH, Wako, 100%) and cellulose nanocrystals (obtained from Luxemburg) were used without further purification. Generally, in this experiment Mill-Q water under 18.2 MΩ were used. Cellulose nanocrystals (CNCs) were extracted from pure ramie fibers as previously reported.[45]

Synthesis of CNCs photonic films

CNCs photonic films were prepared by evaporation induced self-assembly (EISA) method under ambient conditions. Typically, 5 mL of diluted aqueous CNCs suspension (1 wt%, pH=6) were mixed with different amounts of D-glucose (0, 10, 20, 30, 40, 50 and 60 mg), followed by sonication (BRANSON 2800) for 10 minutes. Sonication was performed in an ice bath to maintain the temperature between 22-25 ºC to avoid any desulfation of the CNC surface caused by heating the suspension. The EISA method was then applied by pouring the mixtures onto petri dishes and left at room temperature to evaporate the water for 23 hours.

Preparation of stable aqueous Titania sol

An aqueous stable and transparent titania sol was prepared by modifying the procedure reported by Okunaka et al.[46] Briefly, an appropriate amount of TTiP (weight ratio of TTiP/CNCs is fixed at 1wt%) was added dropwise to an acetyl acetone (acac) solution dropwise by stirring for 10 minutes at room temperature. The prepared TTiP-acac solution was added to a 1 mL aqueous acetic acid solution (AcOH, 3.48 $mol.L^{-1}$) and stirred during 1 h to obtain a transparent titania sol. It is worth to note that such solution remains stable without any white precipitate, even after several weeks. The high stability over time of the precursor solution guarantees the reproducibility for the elaboration of nanostructured films.

Synthesis of mesoporous TiO_2 with a chiral nematic structure ($CNTiO_2$)

Chiral nematic-CNC films were used as biotemplates to prepare TiO_2/CNCs nanocomposite films via an impregnation method. To this end, a CNC-based film was dipped into titania sol for 10 minutes and then dried for 20 minutes at room temperature. Gentle drying reduces film cracking due to the shrinkage of the films during solvent evaporation. This steps was repeated for 8 cycles before heating the films to 70 ºC for 2 h. The cellulose nanocrystal biotemplate was then removed by calcination at higher temperature. Specifically, the TiO_2/CNC composite films were heated at a rate of 2 $°C.min^{-1}$ to 100 °C, and

maintained at this temperature for 2 h, then raised to 500 °C at 2 °C.min^{-1} (AAF1107-230SN-Carbolite) and kept for a further 4 h. Then, the obtained films were gently cooled down to room temperature and were referred to as CNTiO$_2$-X (with X the amount of D-glucose) thereafter. In order to compare the photocatalytic properties of these CNTiO$_2$-X films, we also prepared mesoporous TiO$_2$/CNCs composite as a reference film material by using a similar procedure as described above but in a one-pot step. The same amount and concentration (5 mL, 1 wt %) of CNC were used. To this solution, D-glucose (20 mg) was added, followed by sonication for 10 minutes. Unlike the preparation of CNTiO$_2$-X films, the titania sol, prepared as reported above, was mixed directly with the CNCs solution upon stirring for 1 hour at room temperature. This mixture was then poured into petri dishes and left at ambient conditions to evaporate the solvent. Finally, the biotemplate was removed following the same calcination procedure as described above.

Growth of gold nanoparticles in TiO$_2$ films

The growth of gold nanoparticles (AuNPs) on mesoporous films was performed, following the procedure described previously.[47] Typically, 10 mg of CNTiO$_2$-20 film were soaked in 5 mL aqueous solutions of HAuCl$_4$ (51 µL of 10 mM HAuCl$_4$ in 5 mL water) for 1 h (the weight ratio of Au/TiO$_2$ was fixed at 1 wt%). Afterwards, the films were recovered, washed several times with water and ethanol, and then dried under ambient conditions. The reduction of the gold precursor was achieved by soaking the films in 10 mL of a freshly prepared NaBH$_4$ (aq) solution (200 mM) for 1 h. The resulting composite was washed several times with water and ethanol to remove nanoparticles deposited on the surface of the films, and dried under ambient conditions.

Materials Characterization

The textures of film samples were recorded by polarising optical microscopy (POM) between crossed polarizers on a Zeiss Axio-Observer equipped with a Sony Cyber-shot DSC-W570. Quantitative image analyses were performed for each image using ZEN software 3.2 lite. Measurements of films cross-sections were carried out by Scanning Electron Microscopy (SEM). SEM images were acquired with a ZEISS Supra 55VP FEG-SEM operating at 2 kV and using a working distance between 3 and 5.7 mm. The morphology of mesoporous TiO$_2$ films were studied by Transmission Electron Microscopy (TEM, JEOL JEM 2100Plus), operating at 200 kV. The films were reduced to very small pieces, which were dispersed in ethanol using ultra-sonication and then drop-casted on carbon-coated copper grids. The grids were dried under N$_2$ flow prior to any measurement.

Optical properties of biotemplated mesoporous TiO$_2$ as well as initial CNC photonic films were determined using UV-vis spectroscopy (model Cary 5000 series, Agilent Technologies) equipped with an integrating sphere for diffuse and total reflection measurements. The reflectance spectra were recorded by mounting the film perpendicular to the beam light. The maximum reflectance were set to 100% using BaSO$_4$ as a reference in a wavelength range between 200 to 800 nm. In the case of AuNPs growth on mesoporous TiO$_2$, the absorbance of the samples was collected using a Cary 4/5 diffuse reflection sphere. The baseline was recorded using a poly(tetrafluoroethylene) reference.

Fourier transform infrared (FTIR) spectra of CNC film, TiO$_2$/CNC composite film, and TiO$_2$ product film were carried out on a FTIR spectrometer (Bruker Vertex 70) equipped with a diamond ATR apparatus (PIKEMIRACLE crystal plate diamond/ZnSe) and a MCT detector. The measurements were performed by placing film samples onto a clean ZnSe diamond plate. For each sample, 100 scans were acquired in the 4000-600 cm^{-1} range with a 4 cm^{-1} spectral resolution.

The crystallinity of the film samples was investigated by X-Ray Scattering (XRS) in transmission mode. XRS measurements on CNCs photonic films were carried out on a copper rotating anode generator ($\lambda_{Cu\ K\alpha}$ = 1.5418 Å, Rigaku Corp., Japan) monochromatized with a multilayer W/Si optics (Osmic) and equipped with a MAR345 detector (150 µm pixel size).[49] For these measurements, the sample-to-detector distance was set to 200 mm, allowing an accessible Q range of 0.15 – 2.7 Å^{-1}. Self-supported films were simply mounted on a goniometer head and the films were kept parallel to the incident X-ray beam. Linear scans were performed along a line perpendicular to the film axis, corresponding to scattering from the hk0 reflections of CNC. In the case of biotemplated mesoporous TiO$_2$ films, measurements were performed at the molybdenum wavelength ($\lambda_{Mo\ K\alpha}$ = 0.711 Å) to prevent fluorescence arising from TiO$_2$. Experiments were carried out on a rotating anode generator (Rigaku Corp., Japan) equipped with a multilayer W/Si mirror (Osmic) providing a monochromatic beam of 1 x 1 mm² at the sample position.[48] Two-dimensional XRS patterns were collected on a MAR345 detector (marXperts GmbH, Germany) with 150 µm pixel size, placed at a sample-to-detector distance of 150 mm. The typical accessible range of scattering vector modulus Q was 0.4–7 Å^{-1} ($Q = 4\pi/\lambda \sin(\theta)$, where λ is the incident wavelength and 2θ is the scattering angle). For these experiments, the samples were reduced in powder form and filled into borosilicate capillary tubes (GLAS, Schönwalde bei Berlin, Germany) of 0.7 mm diameter that were flame-sealed. The scattered intensity I as a function of the scattering vector modulus Q was obtained by angular integration over the 2D scattering patterns using homemade software. The data were corrected for empty cell (glass) scattering.

In both XRS measurements modes, the experimental resolution can be approximated by a Gaussian with Full-Width at Half Maximum (FWHM) ~0.013 Å^{-1}. The crystallite size L, perpendicular to the lattice plane, was estimated by using the Scherrer's equation:[50]

$$L = \frac{0.9\lambda}{\beta \cos\theta} \qquad (1)$$

where λ is the incident wavelength, β the full-width at half-maximum (FWHM) of the X-ray scattering peak in radians and θ the corresponding Bragg angle.

Electronic properties and photocatalytic activity

The electronic properties of the mesoporous TiO$_2$ films were characterized by the Time Resolved Microwave Conductivity (TRMC) technique. TRMC is a convenient and non-destructive

way to probe the dynamics of the photogenerated charge-carriers. The laser pulse (OPO laser, EKSPLA, NT342B tunable from 200 – 2000 nm), used as a source of excitation with parametric oscillator, delivers the full width at half-maximum of one pulse with 8 ns and a frequency of 10 Hz. The incident microwave was generated with a Gunn diode at 30 GHz. The TRMC is an indirect method for the measurement of mobiles charges (mainly electrons since holes are heavier with limited mobility) and their lifetime generated at the surface of a photocatalyst after the laser pulse illumination. Thus, the change in microwave power reflected by the sample after illumination, ΔP(t), is recorded. The microwave power absorbed by the sample can thus be expressed as the difference between the incident and reflected microwave power. The relative power difference, ΔP(t)/P, is directly correlated to the difference of the conductivity Δσ (t), as expressed in equation (2).[51]

$$\frac{\Delta P(t)}{P} = A\Delta\sigma(t) = Ae\sum_i \Delta n_i(t)\mu_i \quad (2)$$

Where, Δn_i (t) is the number of charge-carriers i at time t and μ is the mobility of the charge-carriers. In the present case, all TRMC measurements were conducted under UV light at a 350 nm illumination wavelength and with a light energy density received by the samples set at 1.4 mJ.cm^{-2}.

The experimental setup for photocatalytic tests includes a photoreactor, a UV-vis light (Xenon) lamp (Oriel, 300 W) and an oxygen gas supplier. To assess the photocatalytic activity of synthesized TiO_2 films, the degradation of phenol was monitored, as a model pollutant, under UV-vis light irradiation. The photoactive films were introduced into a 3.5 mL quartz vessel reactor (10 mm diameter) containing an aqueous phenol solution (the photocatalyst concentration was set to 0.012 M) followed by sonication (10 min). The reactive medium was then stirred for 30 minutes in the dark and oxygen gas was bubbled under a fixed flow rate. Then, the reactive medium (aqueous phenol solution, 0.15 M and the film) was irradiated during 2h. An aliquot (0.5 mL) of irradiated sample was collected at different time intervals, followed by centrifugation to eliminate any solid from the solution. The phenol degradation was analyzed by HPLC (Agilent 1260 infinity quaternary liquid chromatograph) equipped with a UV detector set at 260 nm for phenol analysis. The column was an adsorbo-sphere C18 in reverse phase (5 μm, I = 150 mm, i.d. = 4.6 mm, Alltech) combined with an All-Guard cartridge system (7.5 × 4.6 mm, Alltech) for elution at a flow rate of 1 mL.min^{-1}, and the mobile phase was composed of 80% H_2O and 20 % acetonitrile. Star software was used for data acquisition.

The production of H_2 from an aqueous methanol solution was performed in a closed quartz reactor with a nitrogen atmosphere and under vigorous stirring. UV-visible light (Xenon lamp, Oriel, 300 W) was used as an illumination source. For these experiments, 3 mg of each photocatalyst film was suspended in 3 mL of a degassed aqueous solution (6.17 M, 18.5 mmol of methanol), used as a sacrificial agent. The amount of H_2 produced was determined by gas chromatography (GC) on a Bruker Scion gas chromatograph, with a thermal conductivity detector (column, molecular sieve 5 A, 75 m × 0.53 mm i.d.; oven temperature, 50 °C; flow rate= 22.5 mL.min^{-1}; detector temperature= 250 °C; carrier gas, nitrogen).

RESULTS AND DISCUSSION

Acid extraction of CNCs from cellulose fibres enables to obtain CNCs nanorods with ester sulphate (CNC-OSO_3H) on their surface. Since the concentration of the latter is critical for the self-assembly of CNCs rods by electrostatic repulsions,[52] the concentration of CNC–OSO_3H concentration was first determined by conductometric titration with NaOH (supporting information Figure S1). The content of sulfate half-ester was about 26.7 mmol.kg^{-1},[53] which is 13-folds lower than the commercially reported value.[54] This is mainly due to the extended time during the dialysis step used to set the pH of the CNCs' final solution (pH=6). The film, obtained by EISA, remains colourless and transparent without any photonic properties (inset of Figure 1.a). This is confirmed by POM and SEM observations, which do not display the typical fingerprint textures of the chiral nematic structure (Figure 1.a and 1.b). Instead, these observations suggest that the rods remain stacked in a disordered multilayers structure, similar to that reported for CNCs films prepared under acidic conditions.[39] This could obviously be attributed to the low surface concentration of sulfate ester groups. By contrast, the addition of D-glucose to the dilute solution of CNCs leads to the formation of iridescent films with photonic properties (inset of Figure 1.c). The iridescent film indicates that the CNCs are periodically organized. This organization in a helicoidal nematic structure gives rise to photonic band-gap. The periodicity of the chiral nematic structure generates a Bragg reflection for a defined wavelength range (forbidden wavelength), leading to a highly coloured CNC film.[55] SEM images display the characteristic twisted layers of the chiral nematic structure (Figure 1.c). In addition, POM observations under crossed polarizers (Figure 1.d) reveal the occurrence of birefringent domains displaying the typical fingerprint texture of the chiral nematic phase. In order to confirm that the colour arises from the helical arrangement of CNC rods, the samples were observed through left- and right-handed circular polarizers, respectively. As shown in Figure S2 (Supporting Information), these results confirm that the CNCs build a left-handed helix, while the samples remain colourless under observation with the right-handed circular polarizers.

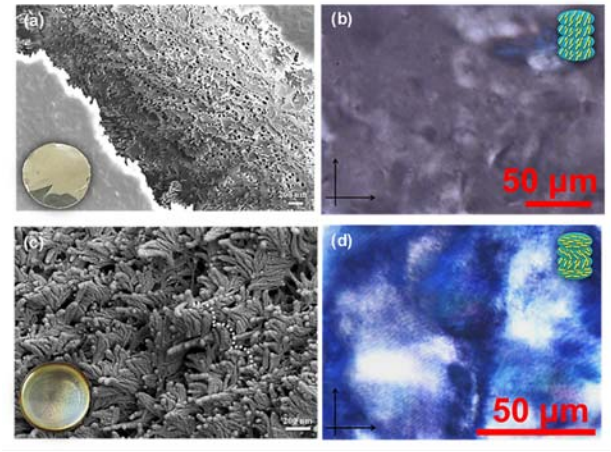

Figure 1. SEM (left), POM (rigth) and macroscopic pictures (inset) of freestanding cellulose nanocrystals films before (a, b) and after (c,d) adding 10 mg of D-glucose. Typical fingreprint texture of the chiral nematic structure is observed after adding D-glucose in POM image (d).

In addition, the as-obtained freestanding films are crack-free. They display a uniform and homogenous colour except at the edges, where colour variation is related to the so called "coffee ring strain", rising from anisotropic kinetics during the solvent evaporation (Figure 2.a).[56] D-glucose has been reported as an efficient strategy to avoid film cracks,[57] but also to control the chiral nematic pitch, and therefore the structural colour of the CNCs films.[58] In our case, the twist is driven by the added amount of D-glucose, which leads to the rotation of CNCs nanorods around helical axis and results in periodic 3D structure. Such an observation has initially been made for a solution of bacterial CNCs that forms a birefringent nematic organization without any chiral nematic fingerprint.[59] However, adding sodium salt to the solution reduces the ionic force at the CNCs surface, which induces the formation of the cholesteric phase. D-glucose could reduce the double electric layer around the CNCs leading to the formation of the helical structure in a similar manner. D-glucose also allows tuning the iridescent colour as well as the wavelength of the Bragg reflection of the photonic films, resulting in biotemplates with various photonic stop-band positions (Figure 2.b). Increasing the amount of D-glucose allows the maximum wavelength of the Bragg reflection to be adjusted from blue (UV), blue-green (UV-visible) to green and red (visible), in agreement with the macroscopic optical observations (Figure 2.a). In contrast, no Bragg reflection was observed for the CNCs film prepared without the addition of D-glucose, confirming the absence of any 3D chiral nematic structure. The CNs is obviously a sinequanone condition to obtain films showing both iridescent colour and a Bragg reflection peak.

The maximum wavelength of the Bragg reflection can be defined as the relationship between the effective refractive index of the films "n_{eff}", the helical pitch "P" and the angle of the helical axis to the emitted light such as:

$$\lambda = n_{eff} P \sin\theta \qquad (3)$$

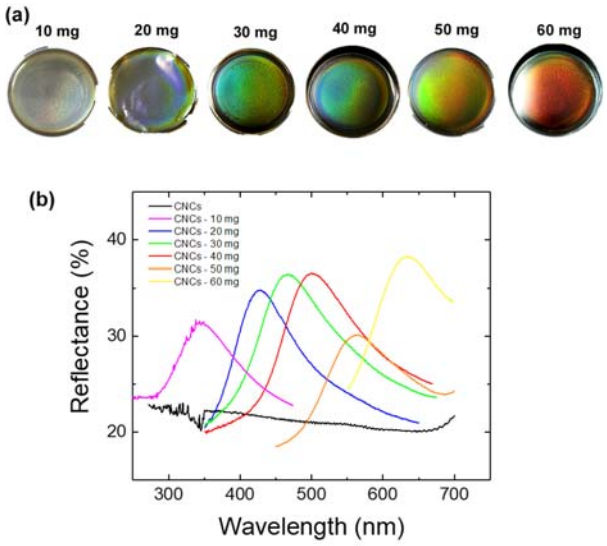

Figure 2. (a) Optical iridescent textures and (b) UV-visible reflectance spectra of CNCs photonic films prepared with different amount of D-glucose.

Since the average refractive index of the CNCs and D-glucose should remain unchanged (CNCs are composed of glucose), the incorporation of D-glucose increases the helical pitch "P" leading to a red-shift of the Bragg peak reflection.

The POM images of the photonic films were obtained under crossed polarizers using non-polarized illumination (Figure 3.a–f). In polarized-light microscopy, the CNCs films prepared with different amount of D-glucose exhibit strong birefringence and multi-domains with random sizes and orientations. This is mainly due to the lack of control of water evaporation and therefore to the fast merging of tactoids in the solution leading to heterogeneous microdomains in the same sample.[60] At the microscopic level, the size of the microdomains, as estimated from the POM images, decreases from 80 to 22 µm with an incorporation of D-glucose from 10 to 60 mg, respectively (Supporting Information Table S1). D-glucose is suspected to increase water retention since hydrophilic interactions through hydrogen bonds are favourable, thereby decreasing the evaporation kinetics of water. In addition, the typical fingerprint of the CN structure is clearly observed regardless of the weight of D-glucose.

The crystallinity of the CNC-films was investigated by X-ray scattering (XRS) measurements (Supporting Information Figure S3). Whatever the glucose content, all XRS diagrams are similar and present three main peaks: A sharp peak located at Q = 1.604 Å^{-1} (d-spacing d = 3.92 Å) and two overlapping peaks at Q = 1.051 Å^{-1} (d = 5.98 Å) and Q = 1.175 Å^{-1} (d = 5.35 Å), corresponding to the $(200), (1\bar{1}0)$ and (110), respectively, characteristics of cellulose I_β.[61,62] The average crystallite size L, perpendicular to the lattice plane, was estimated by using the Scherrer's equation (see Methods section). In addition to adjusting the helical pitch, the incorporation of D-glucose also enhances the average crystallite size by 20% (Supporting Information Table S1).

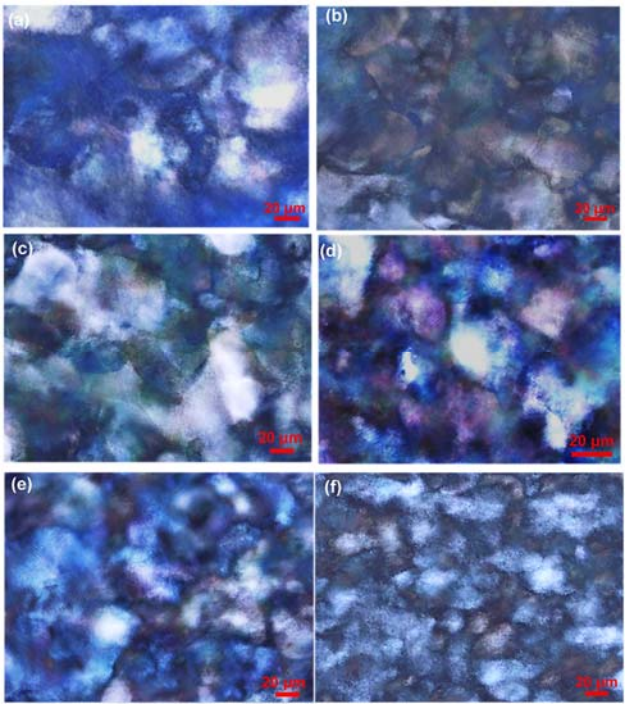

Figure 3 : POM images of CNCs films prepared with (a) 10, (b) 20, (c) 30, (d) 40, (e) 50, and (f) 60 mg of D-glucose.

The successful incorporation of D-glucose is confirmed by SEM observations of the fractured cross-section of the CNCs photonic films (Figure 4). The films present a porous texture when a small amount of D-glucose is added (Figure 4.a–d). Moreover, the characteristic twisted CN structure of CNCs remains observable up to 20 mg of added D-glucose (Figure 4.a–b). At higher glucose content (Figure 4.c–f), the recognition of CNCs and even the chiral nematic structure becomes difficult to identify. These observations confirm that the polyol is inserted into the structure and covers the CNCs nanorods, increasing the helical pitch "*P*" of the chiral nematic structure. This is consistent both with the evolution of the iridescent colour of the films (Figure 2.a) and the red-shift observed for the Bragg peak reflection in Figure 2.b. Altogether, these results confirm the preservation of the CN structure after incorporation of D-glucose.

As a proof of concept of elaborating a mesoporous TiO_2 film with a CN structure, four of the photonic films (CNCs-10, CNCs-20, CNCs-40 and CNCs-60) were impregnated with the titania precursor. After the impregnation step (i.e. the one prepared using 20 mg of D-glucose), the obtained composite ($CNCs/TiO_2$-20) shows a red-shift of the maximum wavelength of the Bragg reflection from λ_{max}=422 nm to λ_{max}=521 nm (Figure 5). The porosity of CNCs photonic films as shown in SEM images (Figure 4) should allow the diffusion of the titania precursor. The colour of the CNCs photonic film turns from blue-green to green-yellow for the composite after impregnation (inset in Figure 5).

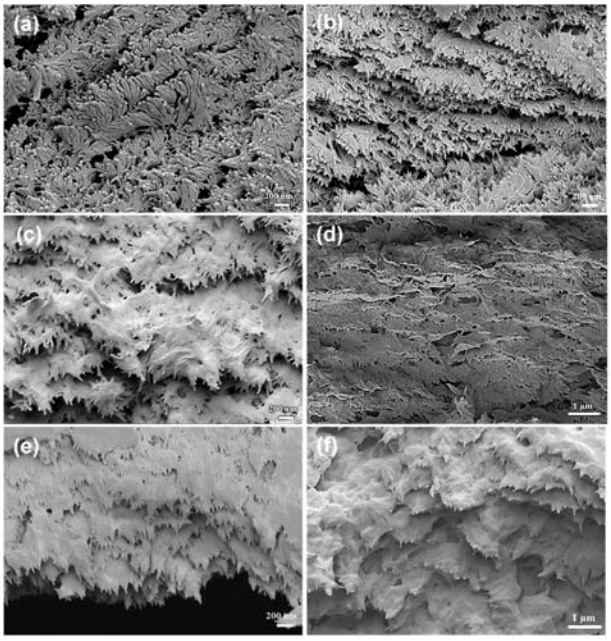

Figure 4. SEM images of the cross section of CNCs photonic films with variable amount of D-glucose: (a) 10, (b) 20, (c) 30, (d) 40, (e) 50, and (f) 60 mg.

Eqn (1) predicts that the Bragg wavelength is red-shifts as the effective refractive index of the films increases. The SEM image of the cross-section of hybrid TiO_2/CNCs-20 film showed that the preservation of the CN structure is similar to that of CNC photonic films (Supporting Information Figure S5). The infiltration of the precursor into the porous film increases the effective refractive index of the medium and, as expected, the spectral position of the Bragg reflection shifts to a higher wavelength (Figure 5). The CNCs are easily removed from the composite films by calcination at 500°C, as evidenced by FTIR analysis (Supporting Information Figure S5) leading to mesoporous TiO_2 films with a preserved CN structure ($CNTiO_2$-20) and a maximum wavelength of the Bragg reflection at λ_{max}=415 nm. POM observation of the film texture is highly birefringent (inset Figure 5), indicating the transfer of the CN structure into the resulting TiO_2 inorganic film. In comparison, mesoporous TiO_2 film prepared by the one-pot method (see method section) presents no birefringence, thus attesting the absence of a cholesteric organization (Supporting Information Figure S6).

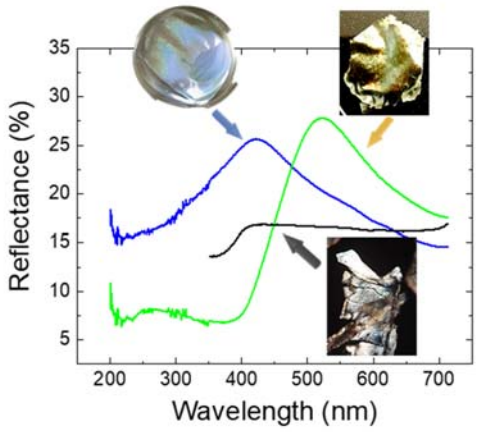

Figure 5. UV-visible reflectance spectra of CNC film with 20 mg of added D-glucose before (CNCs; blue curve) and after impregnation (CNCs/TiO_2; green curve) with TTiP sol. Black curve is collected after the calcination of the nanocomposite CNCs/TiO_2 film. Inserted, the photographic images collected of each sample under normal light (CNCs and CNCs/TiO_2 films) and between crossed polarizers.

The blue shift of λ_{max} upon the removal of CNCs results both from replacing CNCs by void, whose refractive index is lower (r_{CNCs}=1.5)[63] and from the contraction of helical pitch from 2.8 to 1.1 µm (as estimated from POM images). Furthermore, the intensity of the Bragg peak decreases, showing an asymmetric shape. The loss of the symmetry could be related to the collapse of the nanostructure due to crystallization (reorganization of atoms and growth) during the calcination step. The surface of the TiO_2 films was observed by SEM (Supporting Information Figure S7). SEM micrographs display porous structure where the pores are aligned in continuous but variable direction, suggesting a close packing of the CNCs laterally and lengthwise in bundles.[37] This is also confirmed by TEM observation of a fragment of calcined TiO_2 film as shown in Figure 6.a. The TEM micrographs reveal cylindrical-like aligned pores with a diameter of about 4 nm separated by 5 nm of TiO_2 wall. It also shows locally aligned pores, suggesting a localized helical structure. The helical organization is a periodic succession of parallel pores over distances of a few CNC rod diameters and twisted neighbouring pores, which orientation is perpendicular with respect to the electron beam. This result suggests the successful transfer of a localized CN pore structure in the final material.[37,64] Pore sizes smaller than the CNCs diameter measured before impregnation result from distortions caused by the growth of crystallites within the channel walls during calcination.[12] The cylindrical aligned pores are not observed for mesoporous TiO_2 film elaborated from one-pot method (Figure 6.b). Instead, the structure shows only a porous structure, where the pore are randomly distributed. The side view of $CNTiO_2$-20 film with thickness about 6.7 µm after impregnation was further analyzed by SEM (Figure 6.c). The image displays stacked layers that could results from the helical pitch of the photonic films suggesting the transfer of the CN structure to TiO_2 films. Here again, such structure is not observed for the mesoporous TiO_2 sample prepared by the one-pot method (Figure 6.d). Instead, the structure shows a mesoporous structure with a random distribution of the pores and a size distribution in the range of 6–10 nm as deduced from N_2 sorption experiments (see Supporting Information Figure S8). HR-TEM images (Supporting Information Figure S9) evidence a well-crystallized TiO_2 wall with lattice spacing of d=0.32 nm, which can be assigned to (101) interplanar face of the anatase crystalline form. This is confirmed by XRS experiments: The spectra display several peaks corresponding to the anatase form of TiO_2 (Figure 6.e-f). Interestingly, although the microscopic texture of the mesoporous TiO_2 sample is different from that of $CNTiO_2$ films, the XRS pattern is very similar, suggesting that the resulting film structure is highly dependent on the preparation method. Regardless of the photonic films used, the FWHM (Full Width at Half Maximum) measured from the patterns reveals a negligible deviation, suggesting no effect of either the biotemplate nor D-glucose amount on the TiO_2 crystallite size (See Supporting Information Table S1).

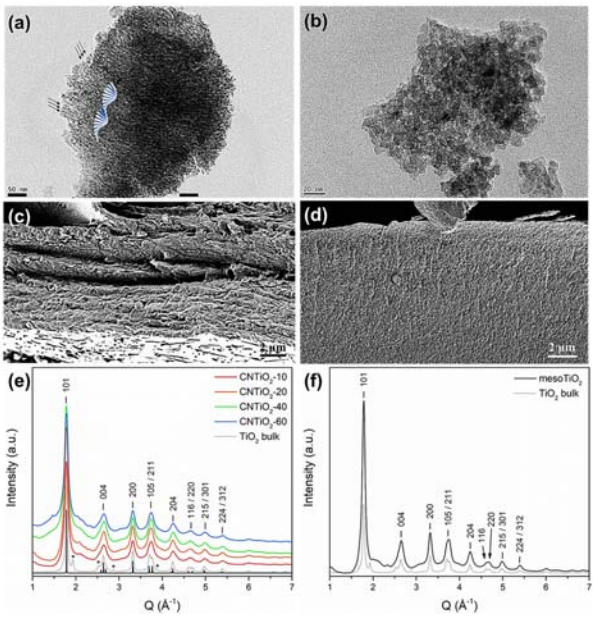

Figure 6. Comparison between samples prepared by (*left*) impregnation ($CNTiO_2$-20) and (*right*) one-pot synthesis (mesoporous TiO_2). (a,b) TEM micrographs and (c,d) SEM observations on the side-view. XRS diagrams of (e) $CNTiO_2$-X obtained with various D-glucose contents and (f) mesoporous TiO_2 samples. The dotted curve corresponds to the XRS diagram of a commercial anatase powder. The black curve in (e) corresponds to the theoretical XRS diagram of anatase (AMCSD card 0019093) while the stars indicate characteristic peaks of rutile form. All curves have been translated for the sake of clarity.

Finally, POM observations were performed on these inorganic films (Figure 7). Mesoporous $CNTiO_2$ samples are strongly birefringent, confirming the anisotropy of the films.[40] At high magnification (Figure 7.e–g), it was possible to clearly identify the typical fingerprint of the CN structure, composed of successive dark and white lines similar to that observed on the initial CNCs photonic films. Our results reveal that it is possible to maintain the chiral nematic structure in the mesoporous films even after calcination. To go further, we will now examine the influence of this peculiar structure on the photocatalytic properties of TiO_2.

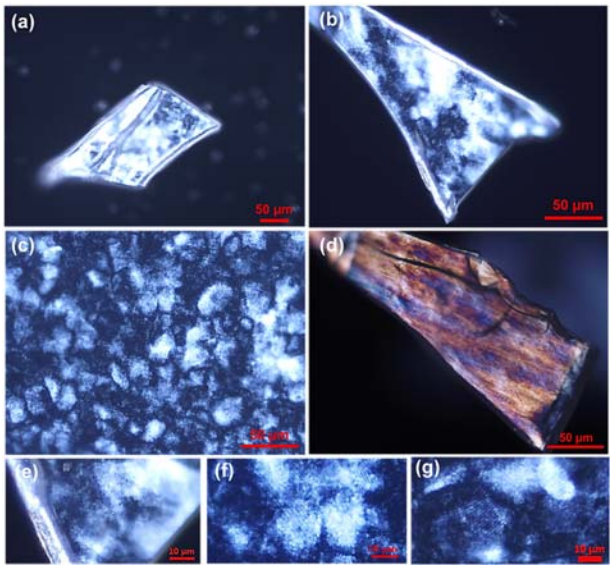

Figure 7. Polarized Optical Microscopy images of mesoporous TiO_2 films obtained from different CNC photonic films: (a) $CNTiO_2$-10, (b) $CNTiO_2$-20, (c) $CNTiO_2$-40 and (d) $CNTiO_2$-60 mg, (e-g) magnification of selected region from (b), (c) and (d) depicting the fingerprint of the chiral nematic structure.

We first investigate the kinetics of photocatalytic reactions, which is closely related to the intrinsic properties of TiO_2, in particular its ability to generate charge carriers upon photoexcitation and transfer them at its surface. Time-resolved microwave conductivity (TRMC) measurements were performed to assess the electronic properties and the effect of the retained CN structure of mesoporous TiO_2 films on the charge carriers' dynamics. TRMC is a contactless technique used for determination of charge carriers' density and their lifetime (transport parameters) in polycrystalline titania.[51] Figure 8.a displays kinetic traces of the transient photoconductivity measured by laser pulsed TRMC excited at 350 nm. The measurements indicate a variation in signal intensity as a function of the amount of D-glucose added in the photonic films. After UV excitation of TiO_2, photogenerated electrons and holes are produced, the electrons are transferred to the surface of $CNTiO_2$, whereas holes heavier than the electrons have limited mobility, and they remain localized at the bulk. The intensity of the TRMC signal is therefore mainly due to mobile photogenerated electrons.[65] The results show an intense TRMC signal (I_{max}) for the films obtained from the mineralization of CNCs photonic films compared to mesoporous TiO_2 film. For instance, the charge carriers' density produced is improved by a factor of 3.5, when the replica of the chiral nematic structure is transferred into $CNTiO_2$-10 films. This improvement is obviously due to the structured mesoporous TiO_2 films. The light scattering in the CN structure allows the confinement of photons, which improves the light harvesting and thus the density of photogenerated charge carriers. The amount of D-glucose does not affect the electronic properties of TiO_2. However, we have shown that the Bragg reflection is shifted to higher wavelength, modifying the position of the red- and blue edges of the stopband of the photonic films, and thus it overlaps with the optical absorbance of TiO_2 (electronic band-gap). Furthermore, the overlap of the electronic excitation wavelength of TiO_2 film ($CNTiO_2$-20 film; Figure 5) with the excitation photon wavelength (350 nm; blue-edge of the Bragg reflection peak) suggests the vanishing group velocity of slow photons. In both cases, we suggest that the CN structure improves the light harvesting properties (optical absorption) of TiO_2 due to a longer photon lifetime in the film, resulting in an increase of the density of photogenerated (e^-/h^+) pairs. Although the I_{max} decreases gradually when the amount of the D-glucose in the initial photonic films increases, it remains significantly higher than in the mesoporous TiO_2 film. The attenuation of the TRMC signal indicates a deactivation of TiO_2 and thus gives information on the lifetime of the photogenerated charge carriers. The lifetime decay is described by both charge recombination, interfacial charge transfer to adsorbed species and default traps.[51,66] It would be difficult to distinguish each pathway from the other to extract quantitative comparison.

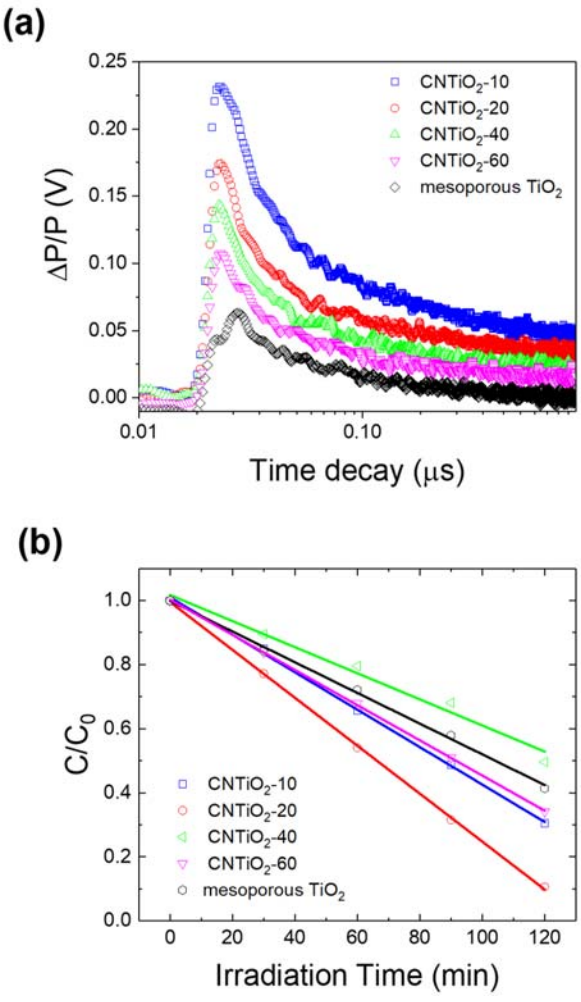

Figure 8. (a) TRMC signal of variable inorganic samples under UV illumination (λ_{ex}=350 nm, I_{ex}=1.4 mJ .cm^{-2}). Photocatalytic degradation of phenol under UV-visible illumination: (b) "C/C_0" plot of phenol concentration as a function of irradiation time for $CNTiO_2$-10, $CNTiO_2$-20, CN-TiO_2-40, $CNTiO_2$-60 and meso-TiO_2.

The photocatalytic efficiency of the films was investigated by following the kinetics of phenol degradation as a probe

molecule. Figure 8.b shows the "C/C_0" plot of concentration of phenol evolution for each samples as a function of illumination time. All mesoporous $CNTiO_2$ films, except for X = 40, display higher photocatalytic activity compared to the pure mesoporous TiO_2 films. This variation cannot be attributed to a difference in crystallite size, since the XRS patterns reveal a negligible deviation suggesting that neither the biotemplate nor D-glucose amount have an effect on the size of TiO_2 crystallites. The thickness of the films, exceeding 1µm for all the films, would not affect the photocatalytic activity, since most of the photogenerated charge carriers produced above 140 nm are thought to recombine before reaching the surface.[67] The photoefficiency is enhanced by a factor of 1.5 for $CNTiO_2$-20, a sample that also shows a match between the illumination energy and absorption of TiO_2. Unfortunately, we were unable to compare the Bragg peak positions due the small size of the films for the other samples. The method used for the synthesis induces the crack of the films in very small pieces due to the stress produced by the shrinkage during the polymerization. However, a "slow photon" effect could not exclusively justify the improvement of the photocatalytic efficiency. Since, the photocatalytic degradation is performed in an agitated system, we had no control over the angle of the incident light reaching the film. Indeed, Wu et al. showed a dependence of the illumination angle on the enhancement of the photocatalytic activity of opal inverse films.[2] The Bragg reflection shifts to higher wavelength, modifying the position of the red- and blue edge of the photonic films stopband, and thus its overlap with the electronic band-gap absorbance of TiO_2. In the reactive medium, the scattering combined to the “slow photon effect” are both responsible for increasing the photogenerated charge carriers, as confirmed by TRMC measurements, and thus for improving the photocatalytic efficiency of phenol degradation. In addition, we also assessed the stability of the materials by performing recycling experiments (see Supporting Information Figure S10). The results indicate a very slight decrease of the efficiency for the phenol degradation after three cycles. This small decrease is due to the loss of a part of the photocatalyst during the recycling tests, since the samples are centrifuged and washed for further use. Nevertheless, the recycling test confirms the photostability of our novel biotemplated TiO_2 films.

To take advantage of the high density of the produced charge carriers for our biotemplated mesoporous TiO_2 films, $CNTiO_2$-20 was coupled with Au nanoparticles (AuNPs) and compared to $mesoTiO_2$ and Au/meso-TiO_2 for H_2 production under UV-vis illumination. AuNPs was extensively studied to extend the absorbance of TiO_2 photocatalyst in the visible range.[3,24] Plasmonic nanoparticles are considered as an efficient electron collector for charge carriers separation, co-catalyst, and light harvesting improvement for hydrogen production.[3,24] A two-step impregnation followed by a chemical reduction method enables growing AuNPs within the pore channels, as revealed by TEM images (Supporting Information, Figure S11 and S12). The chemical reduction performed using ethanoic sodium borohydride ($NaBH_4$) produces a purple solid. The UV-visible absorption spectroscopy displays no absorption in the visible region for $mesoTiO_2$-20 (Figure 9.a). The optical band gap (E_g) of this film was determined using a Tauc plot of modified Kubelka-Munk function with a linear extrapolation (see supporting information Figure S13). The $mesoTiO_2$ sample operates with a band gap (E_g) of 3.18 eV. This value, close to that reported for TiO_2 anatase (3.2 eV), is in agreement with the results obtained from both the XRS analysis (Figure 6.e and f) and the HR-TEM observation (see supporting information Figure S9). TiO_2 in its anatase form (Eg=3.2 eV) absorbs energy only in the UV region, while Au/$mesoTiO_2$-20 and Au/$CNTiO_2$-20 present a broadband absorption in the visible range with maximum wavelength at 547 nm, which is due to the formation of AuNPs (Figure 9.c). AuNPs exhibit localized surface plasmon resonance (LSPR), i.e. collective oscillations of free electrons in response to an incident electromagnetic field. The plasmon-excited energetic electrons (hot electrons) can reduce hydrogen, resulting to the production of H_2. Energy dispersive X-ray analysis indicates that the amount of AuNPs deposited is between 0.1–0.4 wt%. The AuNPs size is estimated from TEM images (see Supporting Information Figure S11 and S12) and ranges from 2.5 to 4 nm, in agreement with the pore size of the film as reported previously. The UV-visible absorption spectrum of Au/$CNTiO_2$-20 confirms the increase in the light harvesting in the visible range (Figure 9.a). As expected, the intensity of the LSPR is enhanced due to multiple light scattering in the $CNTiO_2$ structure. Such an observation, reported for plasmonic opal inverse films and plasmonic core-shell nanostructures, indicates that the enhancement in LSPR intensity could be directly related to an increase of the electromagnetic energy in TiO_2 nanostructures.[24,68,69] Knowing that hot electrons are able to reduce hydrogen ion, hydrogen production is expected to be enhanced. Figure 9.b and 9.c illustrate the kinetics of hydrogen production from an aqueous solution of methanol for different photocatalysts. Methanol was used as a hole scavenger to improve the charge carriers separation, but also to increase the yield of hydrogen generation. TRMC experiments were performed on methanol adsorbed on $CNTiO_2$-20 (supporting information Figure S14). The results indicate a significant decrease in the signal decay when methanol molecules are adsorbed on the surface of the films. This behaviour suggests that holes are trapped by methanol. Methanol reduces e^-/h^+ recombination and improves the separation of charge carriers leading to the increase of the electrons lifetime. This result is consistent with the role that methanol (hole scavenger) usually plays in the photocatalytic production of hydrogen.[70] The H_2 production is significantly improved from 8.1 mmol g^{-1} to 55.2 mmol g^{-1} after 5h with a rate of 1.7 and 13.5 mmol h^{-1} g^{-1}, when Au is loaded in $mesoTiO_2$. AuNPs are necessary to reduce the H^+ formed as a result of the dissociative adsorption of methanol, which is also a well-known sacrificial electron donor.[70,71] The hydrogen production using Au-loaded $CNTiO_2$-20 is eight times higher compared to Au loaded meso-TiO_2 composites after 5h with a rate of 468 mmol h^{-1} g^{-1}. The photonic efficiency of the reaction was also determined in order to compare our samples for hydrogen production (see supporting information for details). Under illumination, the same evolution of the photonic efficiency could be observed when comparing different photocatalyst films. The maximum value of 0.2% was obtained for Au/$CNTiO_2$-20, which is four times higher than the photonic efficiency for Au/$mesoTiO_2$ (0.05%). Compared to the metal-free film, Au/$CNTiO_2$-20 showed an improvement of 31 times with respect to the $mesoTiO_2$ (0.0064%). The chemically amplified photochemistry is attributed to the enhancement of

the light harvesting. These results are in accordance with the TRMC measurements, which show a higher efficiency of charge carriers' generation for nanostructured photocatalysts.

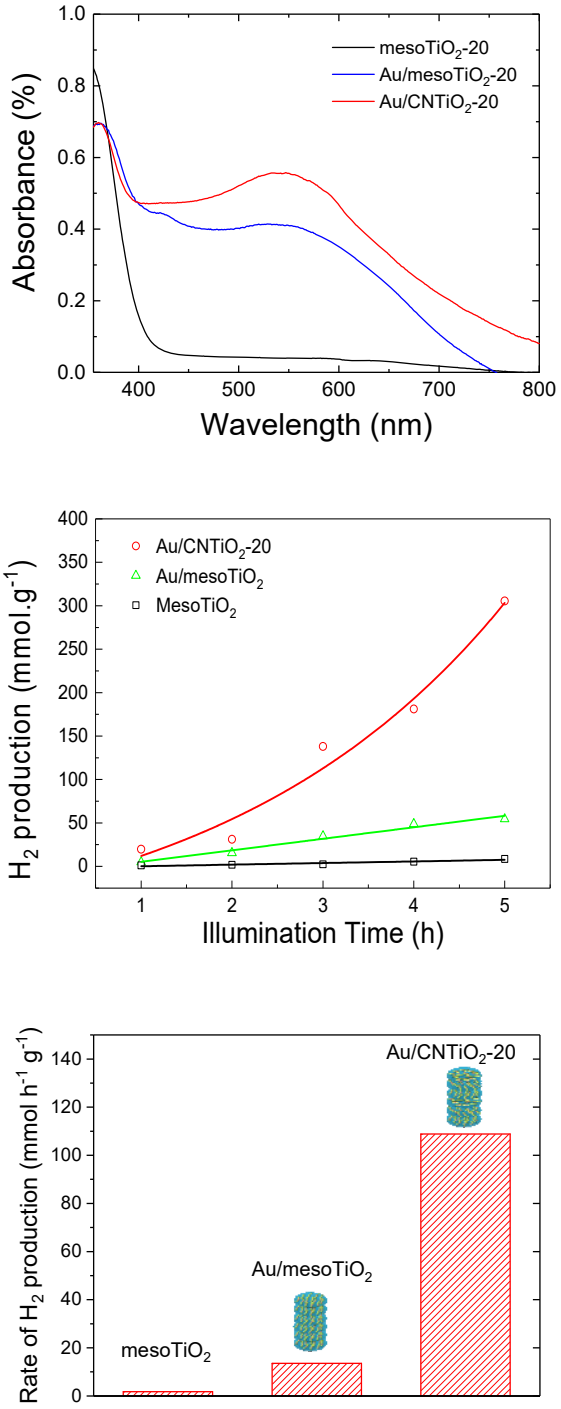

Figure 9. (a) UV-visible absorbance spectra of mesoTiO$_2$, Au/mesoTiO$_2$ and Au/CNTiO$_2$-20 films, (b) evolution of the H_2 production versus the illumination time and (c) rate of H_2 production for mesoTiO$_2$, Au/mesoTiO$_2$ and Au/CNTiO$_2$-20 films. All are normalized per unit of the amount of the photocatalyst.

Conclusion

In summary, we used photonic films of cellulose nanocrystals as biotemplates to replicate the chiral nematic structure into TiO_2 film. We observed that the incorporation of D-glucose in the CNC solution induces a twist of the nanorods leading to the formation of the cholesteric structure. D-glucose, incorporated around and between the CNCs, increases the pitch of the helical structure. We clearly evidence that the impregnation method followed by the calcination step does not alter the CN structure, which is preserved in the resulting CNTiO$_2$ films. Starting from these peculiar structures, TRMC analysis reveals an enhancement of the photogenerated charge carriers' density, which is related to an improvement of the light harvesting performance induced by multiple light scattering effects in the chiral nematic structure. The density of photogenerated charge carriers varies following the optical band-gap of the biotemplate suggesting a slow photon effect. The photocatalytic activity of mesostructured TiO_2 was also found to be much higher than that of mesoporous TiO_2 for phenol degradation and hydrogen production. This approach can be extended to improve the light harvesting from various materials, where the photon-to-energy conversion is a challenge, such as perovskites, g-C_3N_4, Graphene, ZnO or conducting polymers to cite a few. The improvement in the light harvesting capactiy of the chiral nematic structure retained in our mesoporous TiO_2 films should also be promising for Dye Sensitized Solar Cells applications.

ASSOCIATED CONTENT

Supporting Information. Conductimetric titration curve of pristine CNCs, additional characterization of film samples by POM, XRS, FTIR, SEM, TEM and N_2. This material is available free of charge via the Internet at http://pubs.acs.org.

AUTHOR INFORMATION

Corresponding Author

* mohamed-nawfal.ghazzal@u-psud.fr,
Tel: +33 1 69 15 56 02
Laboratoire de Chimie Physique
UMR8000 - Université Paris-Sud, Université Paris-Saclay
Bâtiment 349 - Campus d'Orsay
15, avenue Jean Perrin
91405 Orsay, France

Author Contributions

All authors have given approval to the final version of the manuscript.

ACKNOWLEDGMENT

MNG is grateful to Marie-Claire Schanne-Klein from "Laboratoire d'Optique et Biosciences" for the full access to the polarized optical microscope and for her help on performing the experiments. The authors thank Patricia Beaunier and François Brisset for performing the TEM and SEM images.

REFERENCES

(1) Guillard, C.; Baldassare, D.; Duchamp, C.; Ghazzal, M. N.; Daniele, S. Photocatalytic Degradation and Mineralization of a Malodorous Compound (Dimethyldisulfide) Using a Continuous Flow Reactor. *Catal. Today* **2007**, *122* (1–2), 160–167.

(2) Wu, M.; Jin, J.; Liu, J.; Deng, Z.; Li, Y.; Deparis, O.; Su, B.-L. High Photocatalytic Activity Enhancement of Titania Inverse Opal Films by Slow Photon Effect Induced Strong Light Absorption. *J. Mater. Chem. A* **2013**, *1* (48), 15491.

(3) Méndez-Medrano, M. G.; Kowalska, E.; Lehoux, A.; Herissan, A.; Ohtani, B.; Rau, S.; Colbeau-Justin, C.; Rodríguez-López, J. L.; Remita, H. Surface Modification of TiO_2 with Au Nanoclusters for Efficient Water Treatment and Hydrogen Generation under Visible Light. *J. Phys. Chem. C* **2016**, *120* (43), 25010–25022.

(4) Tétreault, N.; Grätzel, M. Novel Nanostructures for next Generation Dye-Sensitized Solar Cells. *Energy Environ. Sci.* **2012**, *5* (9), 8506.

(5) O'Regan, B.; Gratzel. M. A low-cost, high-efficiency solar cell based on dye-sensitized colloidal TiO_2 films. *Nature* **1991**, *353*, 737–740.

(6) Nishimura, S.; Abrams, N.; Lewis, B. A.; Halaoui, L. I.; Mallouk, T. E.; Benkstein, K. D.; Van de Lagemaat, J.; Frank, A. J. Standing Wave Enhancement of Red Absorbance and Photocurrent in Dye-Sensitized Titanium Dioxide Photoelectrodes Coupled to Photonic Crystals. *J. Am. Chem. Soc.* **2003**, *125* (20), 6306–6310.

(7) Ghazzal, M. N.; Deparis, O.; De Coninck, J.; Gaigneaux, E. M. Tailored Refractive Index of Inorganic Mesoporous Mixed-Oxide Bragg Stacks with Bio-Inspired Hygrochromic Optical Properties. *J. Mater. Chem. C* **2013**, *1* (39), 6202–6209.

(8) Deparis, O.; Ghazzal, M. N.; Simonis, P.; Mouchet, S.; Kebaili, H.; De Coninck, J.; Gaigneaux, E. M.; Vigneron, J. P. Theoretical Condition for Transparency in Mesoporous Layered Optical Media: Application to Switching of Hygrochromic Coatings. *Appl. Phys. Lett.* **2014**, *104* (2), 023704.

(9) Choi, S. Y.; Mamak, M.; von Freymann, G.; Chopra, N.; Ozin, G. a. Mesoporous Bragg Stack Color Tunable Sensors. *Nano Lett.* **2006**, *6* (11), 2456–2461.

(10) Ghazzal, M. N.; Joseph, M.; Kebaili, H.; De Coninck, J.; Gaigneaux, E. M. Tuning the Selectivity and Sensitivity of Mesoporous Dielectric Multilayers by Modifiying the Hydrophobic–hydrophilic Balance of the Silica Layer. *J. Mater. Chem.* **2012**, *22* (42), 22526–22532.

(11) Barhoum, M.; Morrill, J. M.; Riassetto, D.; Bartl, M. H. Rapid Sol–Gel Fabrication of High-Quality Thin-Film Stacks on Planar and Curved Substrates. *Chem. Mater.* **2011**, *23* (23), 5177–5184.

(12) Ghazzal, M. N.; Deparis, O.; Errachid, a.; Kebaili, H.; Simonis, P.; Eloy, P.; Vigneron, J. P.; De Coninck, J.; Gaigneaux, E. M. Porosity Control and Surface Sensitivity of Titania/Silica Mesoporous Multilayer Coatings: Applications to Optical Bragg Resonance Tuning and Molecular Sensing. *J. Mater. Chem.* **2012**, *22* (48), 25302–25310.

(13) Kouamé, N. A.; Alaoui, O. T.; Herissan, A.; Larios, E.; José-Yacaman, M.; Etcheberry, A.; Colbeau-Justin, C.; Remita, H. Visible Light-Induced Photocatalytic Activity of Modified Titanium(iv) Oxide with Zero-Valent Bismuth Clusters. *New J. Chem.* **2015**, *39* (3), 2316–2322.

(14) Kundys, B.; Viret, M.; Colson, D.; Kundys, D. O. Light-Induced Size Changes in $BiFeO_3$ Crystals. *Nat. Mater.* **2010**, *9* (10), 803–805.

(15) Asahi, R.; Morikawa, T.; Ohwaki, T.; Aoki, K.; Taga, Y. Visible-Light Photocatalysis in Nitrogen-Doped Titanium Oxides. *Science* **2001**, *293* (5528), 269–271.

(16) Liu, M.; Qiu, X.; Miyauchi, M.; Hashimoto, K. Energy-Level Matching of Fe(III) Ions Grafted at Surface and Doped in Bulk for Efficient Visible-Light Photocatalysts. *J. Am. Chem. Soc.* **2013**, *135* (27), 10064–10072.

(17) Méndez-Medrano, M. G.; Kowalska, E.; Lehoux, A.; Herissan, A.; Ohtani, B.; Bahena, D.; Briois, V.; Colbeau-Justin, C.; Rodríguez-López, J. L.; Remita, H. Surface Modification of TiO_2 with Ag Nanoparticles and CuO Nanoclusters for Application in Photocatalysis. *J. Phys. Chem. C* **2016**, *120* (9), 5143–5154.

(18) Liu, M.; Inde, R.; Nishikawa, M.; Qiu, X.; Atarashi, D.; Sakai, E.; Nosaka, Y.; Hashimoto, K.; Miyauchi, M. Enhanced Photoactivity with Nanocluster-Grafted Titanium Dioxide Photocatalysts. *ACS Nano* **2014**, *8* (7), 7229–7238.

(19) Hu, M.; Chen, J.; Li, Z.-Y.; Au, L.; Hartland, G. V.; Li, X.; Marquez, M.; Xia, Y. Gold Nanostructures: Engineering Their Plasmonic Properties for Biomedical Applications. *Chem. Soc. Rev.* **2006**, *35* (11), 1084.

(20) Zhang, j.; Jin, X.; Morales-Guzman, P. I.; Yu, X.; Liu, H.; Zhang, H.; Razzari, L.; Claverie, J. P. Engineering the Absorption and Field Au−TiO_2 Whispering Gallery Mode. *ACS nano*. **2016**, 10 (4), 4496–4503.

(21) Zhang, X.; Liu, Y.; Lee, S.-T.; Yang, S.; Kang, Z. Coupling Surface Plasmon Resonance of Gold Nanoparticles with Slow-Photon-Effect of TiO_2 Photonic Crystals for Synergistically Enhanced Photoelectrochemical Water Splitting. *Energy Environ. Sci.* **2014**, *7* (4), 1409.

(22) Seh, Z. W.; Liu, S.; Low, M.; Zhang, S. Y.; Liu, Z.; Mlayah, A.; Han, M. Y. Janus Au-TiO_2 Photocatalysts with Strong Localization of Plasmonic near-Fields for Efficient Visible-Light Hydrogen Generation. *Adv. Mater.* **2012**, *24* (17), 2310–2314.

(23) Bessekhouad, Y.; Chaoui, N.; Trzpit, M.; Ghazzal, N.; Robert, D.; Weber, J. V. UV–vis versus Visible Degradation of Acid Orange II in a Coupled CdS/TiO_2 Semiconductors Suspension. *J. Photochem. Photobiol. A Chem.* **2006**, *183* (1–2), 218–224.

(24) Gesesse, G.D.; Le Neel, T.; Cui, Z.; Bachelier, G.; Remita, H.; Colbeau-Justin, C.; Ghazzal, M. N. Plasmonic Core-Shell Nanostructure as an Optical Photoactive Nanolens for Enhanced Light Harvesting and Hydrogen Production. *Nanoscale* **2018**, *10*, 20140–20146.

(25) De Lucia, E. H.; Nelson, K.; Vogelmann, T. C.; Smith, W. K. Contribution of Intercellular Reflectance to Photosynthesis in Shade Leaves. *Plant, Cell Environ.* **1996**, *19* (2), 159–170.

(26) Poulson, M. E.; Vogelmann, T. C. Epidermal Focussing and Effects upon Photosynthetic Light-harvesting in Leaves of Oxalis. *Plant. Cell Environ.* **1990**, *13* (8), 803–811.

(27) Li, X.; Fan, T.; Zhou, H.; Chow, S. K.; Zhang, W.; Zhang, D.; Guo, Q.; Ogawa, H. Enhanced Light-Harvesting and Photocatalytic Properties in Morph-TiO_2 from Green-Leaf Biotemplates. *Adv. Funct. Mater.* **2009**, *19* (1), 45–56.

(28) Zhou, H.; Li, X.; Fan, T.; Osterloh, F. E.; Ding, J.; Sabio, E. M.; Zhang, D.; Guo, Q. Artificial Inorganic Leafs for Efficient Photochemical Hydrogen Production Inspired by Natural Photosynthesis. *Adv. Mater.* **2010**, *22* (9), 951–956.

(29) Biró, L. P.; Vigneron, J. P. Photonic Nanoarchitectures in Butterflies and Beetles: Valuable Sources for Bioinspiration. *Laser Photon. Rev.* **2011**, *5* (1), 27–51.

(30) Vukusic, P.; Sambles, J. R. Photonic Structures in Biology. *Nature* **2003**, *424* (6950), 852–855.

(31) Vignolini, S.; Rudall, P. J.; Rowland, A. V.; Reed, A.; Moyroud, E.; Faden, R. B.; Baumberg, J. J.; Glover, B. J.; Steiner, U. Pointillist Structural Color in Pollia Fruit. *Proc. Natl. Acad. Sci.* **2012**, *109* (39), 15712–15715.

(32) Deparis, O.; Rassart, M.; Vandenbem, C.; Welch, V.; Vigneron, J. P.; Lucas, S. Structurally Tuned Iridescent Surfaces Inspired by Nature. *New J. Phys.* **2008**, *10* (1), 013032.

(33) Vigneron, J.; Pasteels, J.; Windsor, D.; Vértesy, Z.; Rassart, M.; Seldrum, T.; Dumont, J.; Deparis, O.; Lousse, V.; Biró, L.; et al. Switchable Reflector in the Panamanian Tortoise Beetle Charidotella Egregia (Chrysomelidae: Cassidinae). *Phys. Rev. E* **2007**, *76* (3), 031907.

(34) Chen, J. I. L.; von Freymann, G.; Choi, S. Y.; Kitaev, V.; Ozin, G. A. Slow Photons in the Fast Lane in Chemistry. *J. Mater. Chem.* **2008**, *18* (4), 369–373.

(35) Chen, J. I. L.; Loso, E.; Ebrahim, N.; Ozin, G. A. Synergy of Slow Photon and Chemically Amplified Photochemistry in Platinum Nanocluster-Loaded Inverse Titania Opals. *J. Am. Chem. Soc.* **2008**, *130* (16), 5420–5421.

(36) Guldin, S.; Hüttner, S.; Kolle, M.; Welland, M. E.; Müller-Buschbaum, P.; Friend, R. H.; Steiner, U.; Tétreault, N. Dye-Sensitized Solar Cell Based on a Three-Dimensional Photonic

Crystal. *Nano Lett.* **2010**, *10* (7), 2303–2309.

(37) Dujardin, E.; Blaseby, M.; Mann, S. Synthesis of Mesoporous Silica by Sol–gel Mineralisation of Cellulose Nanorod Nematic Suspensions. *J. Mater. Chem.* **2003**, *13* (4), 696–699.

(38) Shopsowitz, K. E.; Qi, H.; Hamad, W. Y.; MacLachlan, M. J. Free-Standing Mesoporous Silica Films With Tunable Chiral Nematic Structures. *Nature* **2010**, *468* (7322), 1–7.

(39) Shopsowitz, K. E.; Kelly, J. A.; Hamad, W. Y.; MacLachlan, M. J. Biopolymer Templated Glass with a Twist: Controlling the Chirality, Porosity, and Photonic Properties of Silica with Cellulose Nanocrystals. *Adv. Funct. Mater.* **2014**, *24* (3), 327–338.

(40) Shopsowitz, K. E.; Stahl, A.; Hamad, W. Y.; MacLachlan, M. J. Hard Templating of Nanocrystalline Titanium Dioxide with Chiral Nematic Ordering. *Angew. Chemie - Int. Ed.* **2012**, *51* (28), 6886–6890.

(41) Chu, G.; Feng, J.; Wang, Y.; Zhang, X.; Xu, Y.; Zhang, H. Chiral Nematic Mesoporous Films of ZrO_2:Eu(3+): New Luminescent Materials. *Dalton Trans.* **2014**, *43* (41), 15321–15327.

(42) Ghazzal, N. M.; Chaoui, N.; Aubry, E.; Koch, A.; Robert, D. A Simple Procedure to Quantitatively Assess the Photoactivity of Titanium Dioxide Films. *J. Photochem. Photobiol. A Chem.* **2010**, *215* (1), 11–16.

(43) Aubry, E.; Ghazzal, M. N.; Demange, V.; Chaoui, N.; Robert, D.; Billard, A. Poisoning Prevention of TiO_2 Photocatalyst Coatings Sputtered on Soda-Lime Glass by Intercalation of SiNx Diffusion Barriers. *Surf. Coatings Technol.* **2007**, *201* (18), 7706–7712.

(44) Li, C.; Paineau, E.; Brisset, F.; Franger, S.; Colbeau-justin, C., Ghazzal, M. N. Photonic Titanium Dioxide Film Obtained from Hard Template with Chiral Nematic Structure for Environmental Application. *Catal. Today* **2019**, in press, doi.org/10.1016/j.cattod.2019.01.030.

(45) Habibi, Y.; Goffin, A. L.; Schiltz, N.; Duquesne, E.; Dubois, P.; Dufresne, A. Bionanocomposites Based on Poly(ε-Caprolactone)-Grafted Cellulose Nanocrystals by Ring-Opening Polymerization. *J. Mater. Chem.* **2008**, *18* (41), 5002–5010.

(46) Okunaka, S.; Tokudome, H.; Hitomi, Y.; Abe, R. Facile Preparation of Stable Aqueous Titania Sols for Fabrication of Highly Active TiO_2 Photocatalyst Films. *J. Mater. Chem. A* **2015**, *3* (4), 1688–1695.

(47) Schlesinger, M.; Giese, M.; Blusch, L. K.; Hamad, W. Y.; MacLachlan, M. J. Chiral Nematic Cellulose–gold Nanoparticle Composites from Mesoporous Photonic Cellulose. *Chem. Commun.* **2015**, *51* (3), 530–533.

(48) Taché, O.; Rouzière, S.; Joly, P.; Amara, M.; Fleury, B.; Thill, A.; Launois, P.; Spalla, O.; Abécassis, B. MOMAC: A SAXS/WAXS Laboratory Instrument Dedicated to Nanomaterials. *J. Appl. Crystallogr.* **2016**, *49* (5), 1624–1631.

(49) Paineau, E.; Amara, M. S.; Monet, G.; Peyre, V.; Rouzière, S.; Launois, P. Effect of Ionic Strength on the Bundling of Metal Oxide Imogolite Nanotubes. *J. Phys. Chem. C* **2017**, *121* (39), 21740–21749.

(50) Holzwarth, U.; Gibson, N. The Scherrer Equation versus the 'Debye-Scherrer Equation'. *Nat. Nanotechnol.* **2011**, *6* (9), 534.

(51) Colbeau-Justin, C.; Kunst, M.; Huguenin, D. Structural Influence on Charge-Carrier Lifetimes in TiO_2 Powders Studied by Microwave Absorption. *J. Mater. Sci.* **2003**, *38* (11), 2429–2437.

(52) Lin, N.; Dufresne, A. Surface Chemistry, Morphological Analysis and Properties of Cellulose Nanocrystals with Gradiented Sulfation Degrees. *Nanoscale* **2014**, *6* (10), 5384–5393.

(53) Beck, S.; Méthot, M.; Bouchard, J. General Procedure for Determining Cellulose Nanocrystal Sulfate Half-Ester Content by Conductometric Titration. *Cellulose* **2015**, *22* (1), 101–116.

(54) Bardet, R.; Belgacem, N.; Bras, J. Flexibility and Color Monitoring of Cellulose Nanocrystal Iridescent Solid Films Using Anionic or Neutral Polymers. *ACS Appl. Mater. Interfaces* **2015**, *7* (7), 4010–4018.

(55) Lagerwall, J. P. F.; Schütz, C.; Salajkova, M.; Noh, J.; Park, J. H.; Scalia, G.; Bergström, L. Cellulose Nanocrystal-Based Materials: From Liquid Crystal Self-Assembly and Glass Formation to Multifunctional Thin Films. *NPG Asia Mater.* **2014**, *6* (1), 1–12.

(56) Deegan, R. D.; Bakajin, O.; Dupont, T. F.; Huber, G.; Nagel, S. R.; Witten, T. A. Capillary Flow as the Causes of Ring Stains from Dried Liquid Drops. *Nature, London* **1997**, *389*, 827–829.

(57) Kelly, J. A.; Yu, M.; Hamad, W. Y.; Maclachlan, M. J. Large, Crack-Free Freestanding Films with Chiral Nematic Structures. *Adv. Opt. Mater.* **2013**, *1* (4), 295–299.

(58) Mu, X.; Gray, D. G. Formation of Chiral Nematic Films from Cellulose Nanocrystal Suspensions Is a Two-Stage Process. *Langmuir* **2014**, *30* (31), 9256–9260.

(59) Araki, J.; Kuga, S. Effect of Trace Electrolyte on Liquid Crystal Type of Cellulose Microcrystals. *Langmuir* **2001**, *17* (15), 4493–4496.

(60) Park, J. H.; Noh, J.; Schütz, C.; Salazar-Alvarez, G.; Scalia, G.; Bergström, L.; Lagerwall, J. P. F. Macroscopic Control of Helix Orientation in Films Dried from Cholesteric Liquid-Crystalline Cellulose Nanocrystal Suspensions. *ChemPhysChem* **2014**, *15* (7), 1477–1484.

(61) Wada, M.; Heux, L.; Sugiyama, J. Polymorphism of Cellulose I Family: Reinvestigation of Cellulose IV_I. *Biomacromolecules* **2004**, *5* (4), 1385–1391.

(62) French, A. D. Idealized Powder Diffraction Patterns for Cellulose Polymorphs. *Cellulose* **2014**, *21* (2), 885–896.

(63) Dumanli, A. G.; Kamita, G.; Landman, J.; van der Kooij, H.; Glover, B. J.; Baumberg, J. J.; Steiner, U.; Vignolini, S. Controlled, Bio-Inspired Self-Assembly of Cellulose-Based Chiral Reflectors. *Adv. Opt. Mater.* **2014**, *2* (7), 646–650.

(64) Asefa, T. Chiral Nematic Mesoporous Carbons from Self-Assembled Nanocrystalline Cellulose. *Angew. Chemie - Int. Ed.* **2012**, *51* (9), 2008–2010.

(65) Tamaki, Y.; Furube, A.; Murai, M.; Hara, K.; Katoh, R.; Tachiya, M. Dynamics of Efficient Electron–hole Separation in TiO_2 Nanoparticles Revealed by Femtosecond Transient Absorption Spectroscopy under the Weak-Excitation Condition. *Phys. Chem. Chem. Phys.* **2007**, *9* (12), 1453–1460.

(66) Martin, S. T.; Herrmann, H.; Choi, W.; Hoffmann, M. R. Time-Resolved Microwave Conductivity. *J. Chem. Soc.* **1994**, *90* (21), 3315–3322.

(67) Tada, H.; and Tanaka, M. Dependence of TiO_2 Photocatalytic Activity upon Its Film Thickness *Langmuir* **1997**, 13, 360-364

(68) Zhang, Z.; Zhang, L.; Hedhili, M. N.; Zhang, H.; Wang, P. Plasmonic Gold Nanocrystals Coupled with Photonic Crystal Seamlessly on TiO_2 Nanotube Photoelectrodes for Efficient Visible Light Photoelectrochemical Water Splitting. *Nano Lett.* **2013**, *13* (1), 14–20.

(69) Dinh, C.-T.; Yen, H.; Kleitz, F.; Do, T.-O. Three-Dimensional Ordered Assembly of Thin-Shell Au/TiO_2 Hollow Nanospheres for Enhanced Visible-Light-Driven Photocatalysis. *Angew. Chemie* **2014**, *126* (26), 6736–6741.

(70) Shen, M.; Henderson, M. A. Identification of the Active Species in Photochemical Hole Scavenging Reactions of Methanol on TiO_2. *J. Phys. Chem. Lett.* **2011**, *2,* 2707–2710.

(71) Tomoji Kawai; Tadayoshi Sakata. Photocatalytic Hydrogen Production. *Chem. Commun.* **1980**, *15*, 694–695.

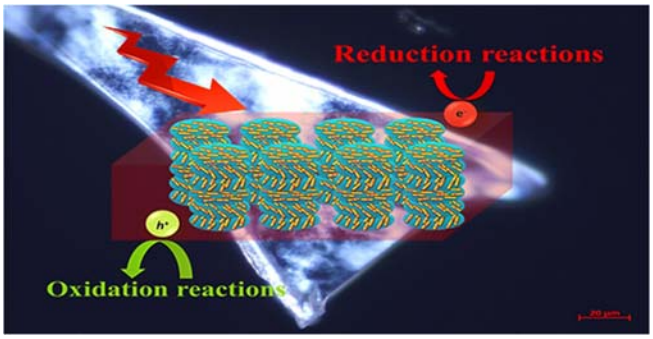
Reduction reactions
e⁻
h⁺
Oxidation reactions